Nano Energy 104 (2022) 107986

Contents lists available at ScienceDirect

Nano Energy

journal homepage: www.elsevier.com/locate/nanoen

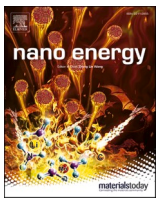

Radially oriented functional thermal materials prepared by flow field-driven self-assembly strategy

Xinfeng Zhang, Bin Xie, Shuling Zhou, Xuan Yang, Yiwen Fan, Run Hu, Xiaobing Luo *

State Key Laboratory of Combustion, School of Energy and Power Engineering, Huazhong University of Science and Technology, Wuhan 430074, China

ARTICLE INFO

Keywords:
Thermal materials
Hotspot
Vacuum filtration
Radially oriented structure
Solar-thermal-electric conversion

ABSTRACT

Filler-reinforced polymer composites are widely applied in thermal management field on account of their promising heat transport ability, superior flexibility and excellent durability. Inside these composites, thermally conductive fillers are usually uniformly distributed or unidirectionally oriented in polymer matrix to improve thermal performances. However, the ever-shrinking and spatially distributed heat sources in three-dimensional, high-density packaged electronic devices have created the localized "hotspot" problem, which raises a new challenge and stricter requirement for the composite thermal materials. Inspired by the amazing radial microstructures in ginkgo leaf, we proposed a flow field-driven self-assembly strategy to fabricate functional thermal materials with radially oriented carbon fibers (CFs). To quantitively evaluate the orientation, an orientation algorithm based on microscale image identification was developed, and an evaluation criterion was proposed. The underlying orientation mechanisms of fillers under the driving of flow field were revealed by visual simulation of vacuum filtration. Thanks to the well-oriented fillers architecture, the composites demonstrated an ultrahigh in-plane thermal conductivity of 35.5 W/(m•K) with a thermal conductivity anisotropy of 19.8, which enables rapid and efficient heat dissipation pathways towards localized hotspots. In addition, this flow field-driven self-assembly strategy provides a promising self-design ability that is expected to solve the heat dissipation of arbitrary-shape heat sources, and shed light on other application scenarios like efficient solar-thermal-electric conversion.

1. Introduction

The artificial composites have been widely applied in people's lives. Polymers are usually used as the matrix of artificial composites because of their promising heat transport ability, superior flexibility, and excellent durability [1–5], which has attracted widespread attentions from thermal [6,7], mechanical [8], biochemistry [9], food scientific [10] and other fields. However, in thermal management field, the application of polymers is usually limited by the low thermal conductivities (TC) of polymers when polymers are used as thermal interface materials (TIMs). Currently, a common strategy to improve the thermal performance of polymer composites is to directly blend kinds of special fillers with polymers, including metal or metal oxides (e.g., Al, Al_2O_3, CuO) [11–13], ceramics (e.g., BN, AlN) [14–18], carbon-based fillers (e.g., Graphene, carbon fibers) [19] and etc. Importantly, besides the attributes of fillers, the macroscopic performance and function of polymer composites depend on fillers' microstructure inside the polymer, especially for anisotropic fillers, such as carbon fibers and hexagonal boron nitride [20]. Thus, a growing number of researches have focused on the microstructural regulation of fillers inside polymers by electrical force [21], magnetic force [22] and shear force [23,24], aiming to manipulate fillers and fabricate vertical and horizontal oriented structures or 3D network [25–27]. These polymer/fillers microstructures bring a remarkable improvement in thermal performance in a specific direction and thus broaden their practical applications, typically in heat dissipation systems [28–30]. However, the development of next-generation 5 G cellular devices and military communications bring new challenges for composite thermal materials [31]. Specifically, the integral chips are becoming miniaturized and exhibit higher power density, up to 300 W/cm^2, even next-generation devices could exceed 1 KW/cm^2 [1]. Besides the power density, the spatial distribution of heat at chip level is also of concern and can have thermal management implications. Localized functional areas in modern chips can incur "hotspot" – regions where local temperatures are significantly higher than the average temperature of chips [1]. The localized accumulation of heat always leads to fast aging or even failure of the core chip because the overall

* Corresponding author.
E-mail address: luoxb@hust.edu.cn (X. Luo).

https://doi.org/10.1016/j.nanoen.2022.107986
Received 28 August 2022; Received in revised form 9 October 2022; Accepted 4 November 2022
Available online 5 November 2022

reliability of the chip is determined by the hottest region on the chip rather than the average temperature [1,32]. Therefore, the heat caused by hotspots needs to be rapidly diffused by targeted and regional-level heat channels, and then dissipated to the environment by the heat sink. The improvement of thermal performance along a specific direction can't solve this problem well. Hence, it's urgently needed to elaborately manipulate the fillers to form special microstructures to provide embedded multidirectional phonon pathways in composites for adapting to the thermal flow field of the hotspot, which remains a challenge.

Fortunately, there are a lot of fantastic microstructures among creatures in nature to meet different requirements, which provide significant inspirations for the designing of artificial thermal materials. For example, the balsa shows a regular circinate structure of the trunk, whose water-delivery xylem vessels grow vertically to ensure sufficient and rapid moisture vertical transportation, as shown in Fig. 1(a-b). In addition, the ginkgo leaf grows the radially aligned microchannels to ensure efficient moisture transportation from the root to the edge of leaves, as shown in Fig. 1(c-d). Similarly, the radial structure of sea urchin shell provides excellent mechanical strength, as shown in Fig. 1 (e). Ingenious natural prototypes undoubtedly provide novel ideas for constructing microstructures in composites [33,34]. For example, nacre-bionic nanocomposite membranes were fabricated by vacuum filtration method, showing superior thermal conductivities and mechanical performances on account of the orderly stacked arrangement [35]. Inspired by these biological structures, we came up with the idea that composites with a radial structure exhibit great potential as TIMs in dealing with the hotspot problem. To realize the rapid and accurate heat transfer for hotspots, we intended to mimic leaves to prepare composites with radially oriented carbon fibers (CFs, one-dimensional material) to utilize their excellent TC in the axial direction. In previous studies, a similar structure has been accomplished and applied in different fields including solar energy collection [36] and water purification and transportation [37] by the multidirectional ice-template assembly method [38,39]. For solar energy collection, radially oriented and overlapped BN forms continuous heat transfer channels, which contributes to the rapid conduction of localized light sources. However, the ice-template assembly method is unsuitable for the preparation of radial structure for one-dimensional materials, because it cannot control the axial orientation of one-dimensional materials such as CFs. To obtain a better orientation of CFs, a more effective method for one-dimensional materials is needed.

Here, we proposed a flow field-driven self-assembly strategy, which combines vacuum filtration method [35,40–42] and fluid control method [43], to prepare thermally conductive composites with radial and centrosymmetric structures. Different from the traditional vacuum filtration setup, a guide plate is designed and placed on the upper flask, to control fluid flow above the filtrating membrane and form the special flow field, which drove the CFs to arrange along the streamlines by the action of shear forces. Combining the vacuum filtration, CFs are blocked and deposited on the filtrating membrane with CFs keeping the regular and special arrangement when the liquid flow through the filtrating membrane, which forms a self-assembly process. Specifically, we

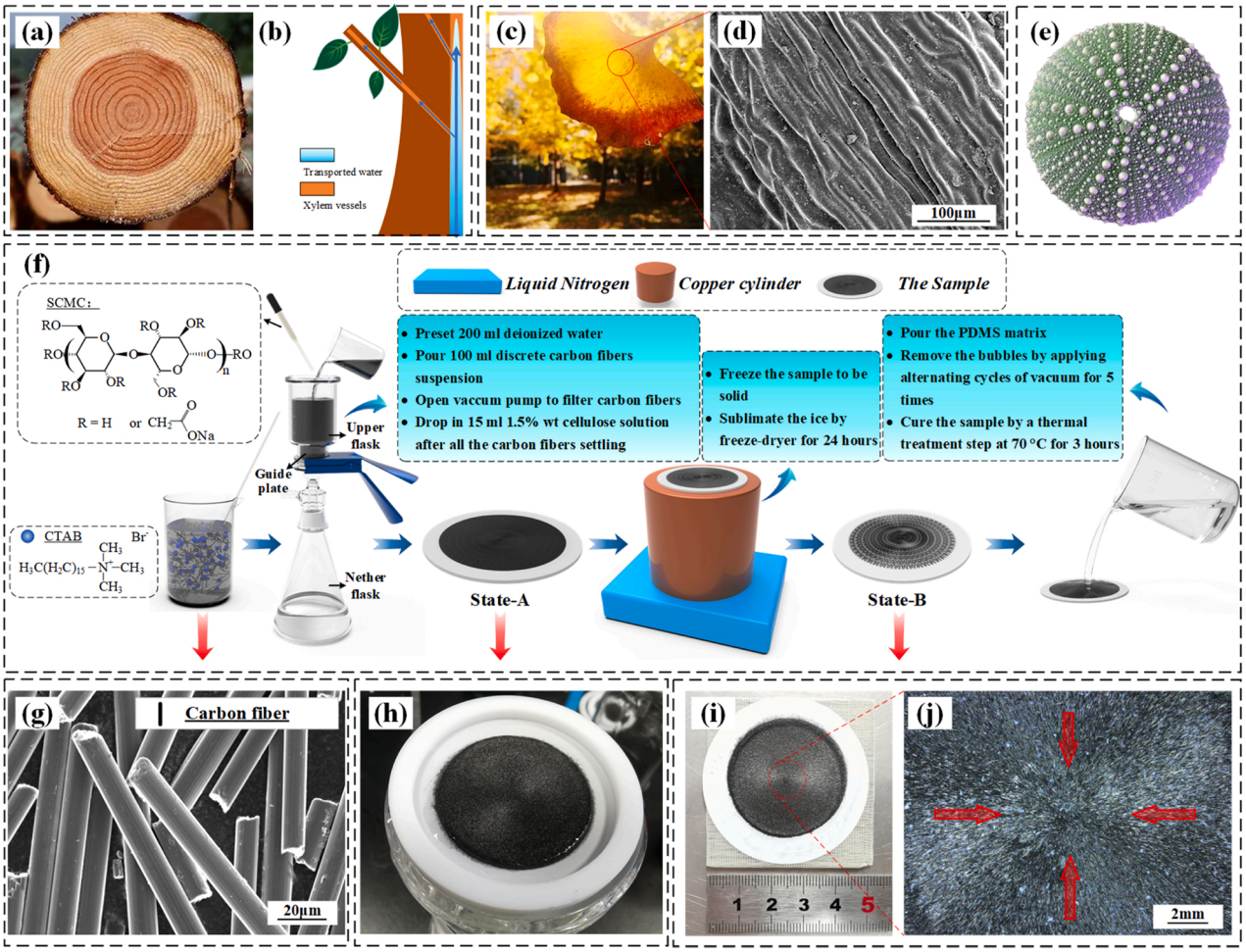

Fig. 1. (a) Optical image of balsa. (b) Diagram illustration of water transportation within trees [36]. (c) Optical image of a ginkgo leaf. (d) Superficial SEM image of a ginkgo leaf. (e) Optical photo of the shell. (f) Schematic diagram for the preparation of composites with radially oriented CFs. (g) SEM image of CFs. Optical photo of state-A (h) after vacuum filtration and state-B (i) after freeze-drying. (j) Optical image of the center of state-B.

prepared radially oriented and centrosymmetric composites (Ra-composites) by designing the guide plate, which are beneficial to the heat diffusion of hotspots. To quantitively evaluate the degree of orientation, we proposed an orientation algorithm based on microscale image identification and an evaluation criterion with no need of X-ray diffraction (XRD) or wide-angle X-ray scattering (WAXS) [25]. In addition, the flow field of vacuum filtration was simulated and analyzed, demonstrating the flow under the guide plate and interpreting the separation phenomenon discovered in experiments. In the Ra-composites, fast, straight-through and efficient phonon pathways are built by the radial arrangement and connection of CFs, which maximally utilizes CFs' anisotropic TC. The Ra-composites exhibit excellent arrangement and ultrahigh in-plane thermal conductivities (in-plane TC) with the highest value reaching 35.5 W/(m•K) (236 times that of pure PDMS (0.15 W/(m•K))), which therefore enables a powerful heat diffusion and uniform temperature distribution when applied in the hotspot. Meanwhile, the highest anisotropy of Ra-composites reaches 19.8, which indicates CFs' anisotropy is fully utilized. Derived from this fast and radially uniform heat-transfer characteristic of radial structure, the hotspot temperature with Ra-composites demonstrated 33.4 ℃ lower than commercial TIMs in the experiment of thermal diffusion for hotspots. Moreover, the heat dissipation system with Ra-composites exhibited a better cooling effect than that with commercial TIMs. Furthermore, this flow field-driven self-assembly strategy demonstrates a promising self-design ability for the arrangement of arbitrary two-dimensional shapes and a promising application in hotspots. Composites with more fantastic arranged structures are expected to be applied in arbitrary-shape heat sources and other fields like solar-thermal-electric conversion.

2. Results and discussion

2.1. Fabrication of the composites

As shown in Fig. 1(g), carbon fibers with the typical one-dimensional structure and high axial thermally conductive characteristic (~600 W/(m•K)), are selected as the basic unit. The flow field-driven self-assembly strategy is intended to engineer the radial architecture, which is schematically illustrated in Fig. 1(f). Given that CFs are poorly dispersed and easy to agglomerate in water, herein, hexadecyl trimethyl ammonium bromide (CTAB, cationic surface-active agent) is first added into CFs suspension, to promote the dispersion of CFs (Fig. S1). After all the CFs are settled in the process of vacuum filtration, sodium carboxymethyl cellulose (SCMC) solution is added into the suspension to fix the CFs. After vacuum filtration finishes, CFs are deposited on the filtrating membrane with SCMC and a small amount of water (state-A), as shown in Fig. 1(h). After freeze-drying by liquid nitrogen in a freeze-dryer, the remaining water is removed with SCMC and CFs remaining (state-B, CFs-scaffold), as shown in Fig. 1(i)(j). The detailed description of composites preparation can be seen in the experiment section. The difference between flow field-driven self-assembly strategy and traditional vacuum filtration method is illustrated in detail in Fig. 2(a)(b). In flow field-driven self-assembly strategy, a guide plate is designed and placed 3 mm above the filtrating membrane to control the flow field, as shown in Fig. 2(a). To form a radial flow field, the guide plate is made into a 2 mm disc with an aperture in the center. The fluid above the guide plate is compelled to flow through the aperture under the negative pressure of the nether flask, then spread out from the center to the edge, which forms the diffusion flow. In this process, CFs are driven to orientate along the streamlines by the shear force of fluid. Simultaneously, the water is pumped out through the filtrating membrane because of the negative pressure in the nether flask, enforcing CFs to be deposited on the filtrating membrane, where CFs maintain the special arrangement. Importantly, the filtrating membrane pore and guide plate aperture can be adjusted to control the flow field above the filtrating membrane and thus determine the arrangement of CFs. A certain amount of whirlpool forming above the diffusion flow doesn't influence the arrangement upon filtrating membrane because the diffusion flow exists until all the CFs are deposited. Ultimately, CFs form a radially oriented structure, resembling the flow field. However, in traditional vacuum filtration

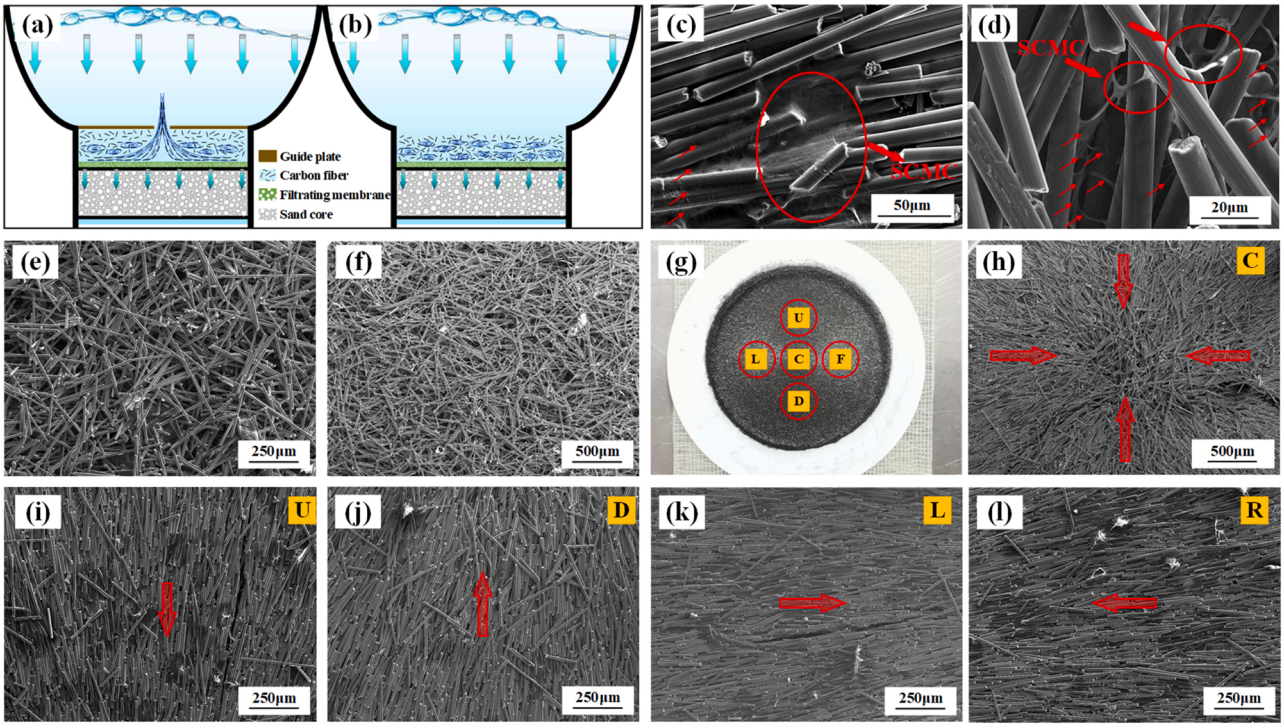

Fig. 2. Schematic diagram of flow field-driven self-assembly strategy (a) and traditional vacuum filtration method (b). (c)(d) SEM images of SCMC binding CFs. (e)(f) SEM images of Ro/0.45/blank-composite in state-B. (g) Optical image of Ra/0.45/5-composite in state-B of different areas. SEM images of the corresponding region of C (h), U (i), D (j), L (k) and R (l) in (g), representing the center, up, down, left and right, respectively.

method, the flow field above filtrating membrane is random and changeful, resulting in random and chaotical deposition of CFs. Herein, Ra/0.45/5-composite was prepared using a filtrating membrane with 0.45 μm pore and a guide plate with 5 mm aperture by flow field-driven self-assembly strategy. For comparison, the Ro/0.45/blank-composite was prepared using 0.45 μm pore filtrating membrane without the guide plate by traditional vacuum filtration method.

Fig. 2(g-l) present the detailed structural information of Ra/0.45/5/composite in state-B. Specifically, Fig. 2(h-l) are the partially enlarged SEM images of the corresponding position related to Fig. 2(g), where C, U, D, L and R represent the center, up, down, left and right, respectively. Obviously, CFs in Ra/0.45/5/composite forms the radial arrangement, in which most of CFs are oriented toward the center. For comparison, the SEM images of Ro/0.45/blank-composite (control group) are shown in Fig. 2(e)(f), where the guide plate is removed with other parameters unchanged. It can be clearly seen from Fig. 2(e)(f) that CFs intermesh chaotically without any order. The reason for the difference between Ra/0.45/5/composite and Ro/0.45/blank-composite is that the guide plate constrains the flow of fluid, forming the diffusion flow under the guide plate. The detailed flow process has been interpreted in the former section. In addition, Fig. 2(c)(d) present the detailed SEM information of SCMC in state-B of Ra/0.45/5-composite. The white SCMC sticks and wraps around the CFs to fix them spatially, protecting the deposited CFs skeleton from damage in the process of matrix filling.

2.2. Selection of the optimal parameters (aperture and pore)

2.2.1. Evaluation of composites' orientation

It is worth noting that, the diameter of aperture will affect the flow velocity of liquid through the aperture, and the filtrating membrane with different pores will determine the overall speed of filtration. Hence, the diameter of aperture and the filtrating membrane pore will influence the flow field above the filtrating membrane, which will influence the arrangement of CFs. To obtain the optimal parameters, we explored the influence of different parameters including the diameter of aperture (5 mm, 7 mm, 9 mm) and the filtrating membrane pore (0.22 μm, 0.45 μm, 0.80 μm). Fig. 3(a-f) presents the upper surface SEM image of composites with six different parameters. It is clear that different degrees of orientation can be observed. To quantitively evaluate the degree of orientation (ORI), an orientation algorithm based on microscale image identification was developed, and an evaluation criterion was proposed. In this evaluation criterion, the degree of orientation in the vertical direction (*V-ORI*) is supposed to evaluate how close the orientation of CFs is to the vertical direction. The process and schematic diagram of calculating *V-ORI* are shown in Fig. 3(i-m) in detail. First, the initial SEM image (Fig. 3(i)) was handled by edge extraction, smoothing and binarization to obtain the binary image (Fig. 3(j)), which was actually a pixel matrix (containing white pixel and black pixel). Fig. 3(k) clearly presents that the white pixels are derived from the edge of CFs because their brightness is different from other locations. Fig. 3(l) presents the three different conditions of CFs. It is interesting that, there are

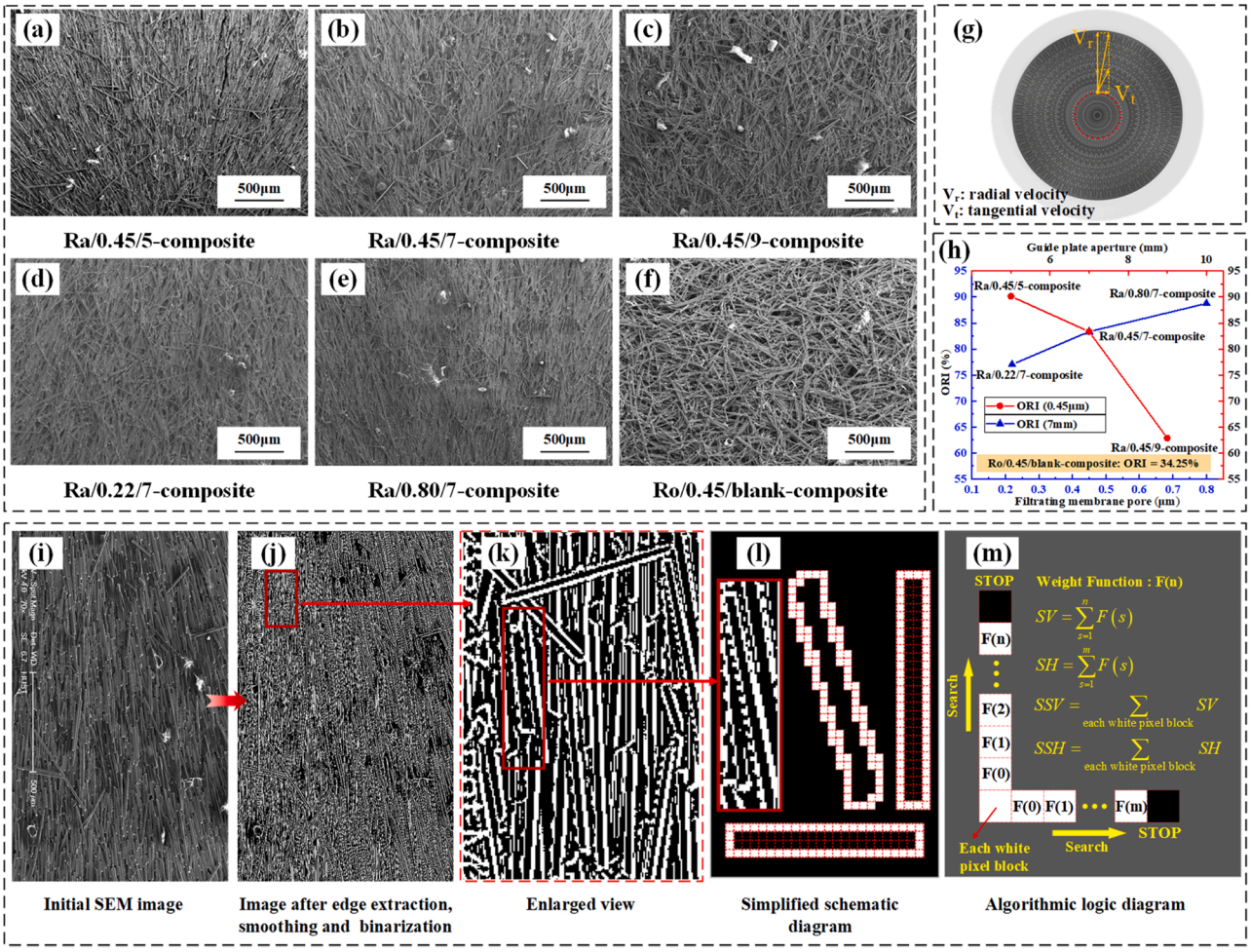

Fig. 3. SEM images of six composites with different parameters, Ra/0.45/5-composite (a), Ra/0.45/7-composite (b), Ra/0.45/9-composite (c), Ra/0.22/7-composite (d), Ra/0.80/7-composite (e), Ro/0.45/blank-composite (f). (g) schematic diagram of radial and tangential velocity. (h) The calculated result of composites' ORI. (i-m) The schematic diagram of calculating *V-ORI* based on microscale image identification.

more continuous white pixels in the vertical direction when CFs are closer to the vertical direction, which is similar to the horizontal direction. According to this rule, the algorithm for calculating ORI is proposed, as shown in Fig. 3(m). For each white pixel (base chunk), the same operation is executed. Specifically, in the vertical and horizontal direction, the pixel blocks on the top and right of the base chunk are traversed and checked whether it is a white pixel step by step upward and rightward until a black pixel is encountered, respectively. The numbers of continuous white pixels are defined as *n* and *m* in the vertical and horizontal directions, respectively. Particularly, the sustainability of base chunk in the vertical and horizontal direction is defined as *SV* and *SH*, respectively, which are calculated with weight function (*F(n)*, defined to expand the discrimination between *SV* and *SH*). Hence, *SV* and *SH* are calculated as follows:

$$SV = \sum_{s=0}^{n} F(s) \text{ and } SH = \sum_{s=0}^{m} F(s) \tag{1}$$

For the binary image, the sustainability of the image in the vertical and horizontal direction is defined as *SSV* and *SSH*, respectively. All the *SV* and *SH* are added up to *SSV* and *SSH*, calculated as follows:

$$SSV = \sum_{each\ white\ pixel\ block} SV \text{ and } SSH = \sum_{each\ white\ pixel\ block} SH \tag{2}$$

It is obviously true that, there are more continuous white pixels in the vertical direction resulting in the larger *SSV* and smaller *SSH* when the CFs are closer to the vertical direction. Hence, *V-ORI* is defined as follows:

$$V-ORI = \left(1 - \frac{SSH}{SSV}\right) \times 100\% = \left(1 - \frac{\sum_{each\ white\ pixel\ block} \sum_{s=0}^{m} F(s)}{\sum_{each\ white\ pixel\ block} \sum_{s=0}^{n} F(s)}\right) \times 100\% \tag{3}$$

To evaluate the real orientation, the *V-ORI(i)* (*V-ORI* of the *(i)*th rotation) is calculated by 180 times, where the initial SEM image is rotated by one angle for each calculation. The maximum of *V-ORI(i)* is regarded as the final ORI. As a result, the ORI and the holistically oriented direction of all CFs can be recognized. The complete flow chart and the selection of weight function are illustrated in Fig. S3 and Fig. S4. The ORI of all composites are calculated and shown in Fig. 3(h). It is worth noticing that the ORI declines with the increase of aperture diameter (the red line with circles). The main reason is that the in-plane diffused velocity (V_i) declines with the increase of aperture diameter. The higher radial velocity makes the resultant velocity tend towards the radial direction when the stochastic disturbance is considered, as shown in Fig. 3(g). Similarly, the ORI increases with the increase of filtrating

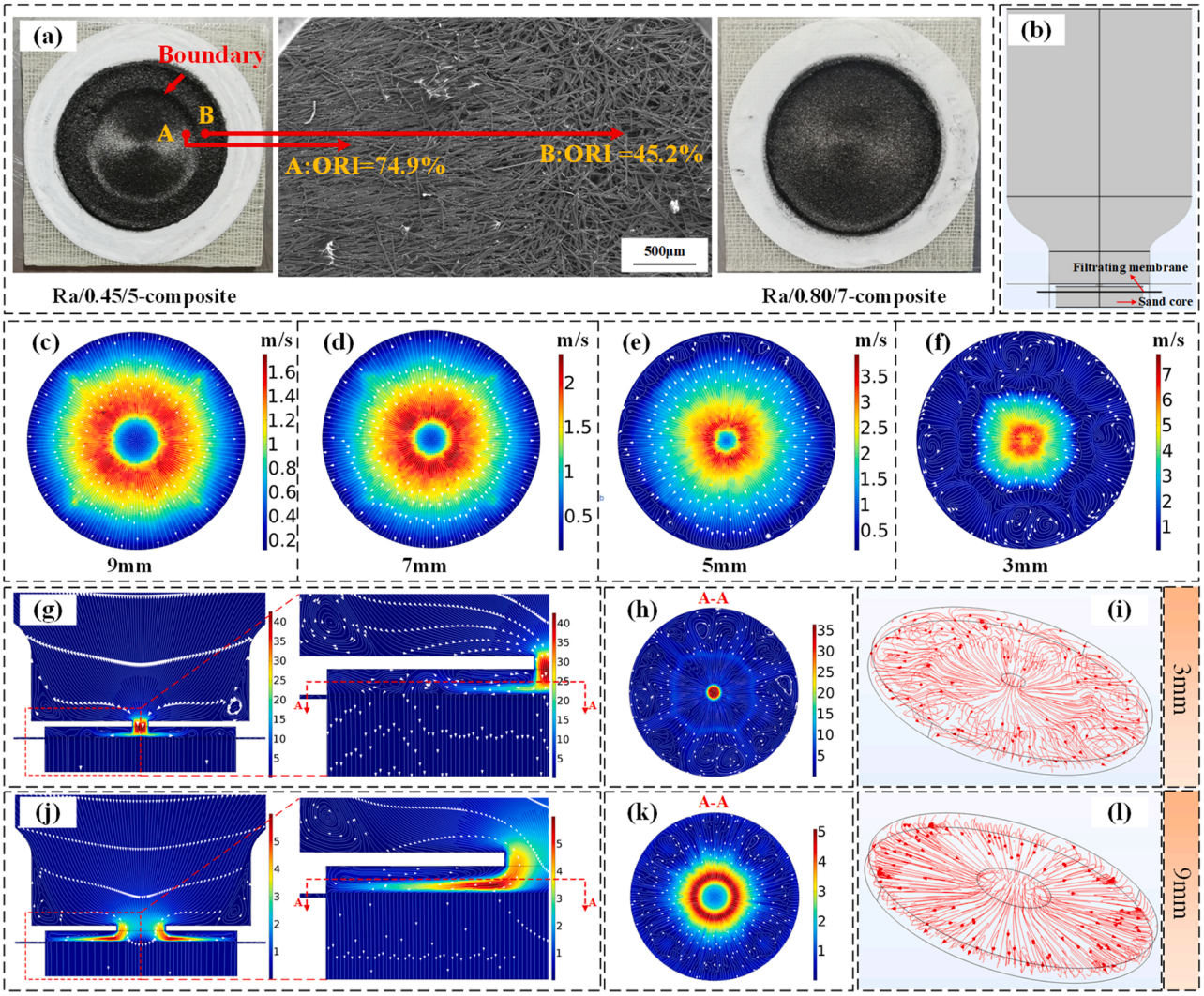

Fig. 4. (a) Separation phenomenon with an obvious boundary. (b) Geometric model of simulation. (c-f) The flow field of different apertures at 0.1 mm above the filtrating membrane. The longitudinal section views and their enlarged views of 3 mm (g) and 9 mm (j). (h)(k) The A-A cross-section views of corresponding position. The streamlines of flow domain above filtrating membrane under the guide plate of 3 mm (i) and 9 mm (l), respectively.

membrane pore (blue line with triangles), because the bigger pore brings less resistance, resulting in larger in-plane diffused velocity. As a result, the diameter of aperture and filtrating membrane pore influence the ORI by impacting the in-plane diffused velocity. In addition, Ro/0.45/blank-composite shows an ORI of 34.25 %. It's hard to accomplish a completely random arrangement (ORI equals 0 %) because the random flow also exists kind of orientation in a small area. However, with respect to the whole area of random composite, no obvious regulation can be discovered in Ro/0.45/blank-composite, as shown in Fig. 3 (f). According to abundant measurements, when the ORI is lower than 40 %, the composite can be regarded as a randomly oriented composite. In addition, the sectional SEM images validate the reliability of the orientation algorithm, as shown in Fig. S7.

2.2.2. Simulation of the self-assembly process

Interestingly, it is clearly observed that, different from Ra/0.80/7-composite, an obvious boundary occurred in Ra/0.45/5-composite, which distinguishes two regions with different ORI (separation phenomenon), as shown in Fig. 4(a). In the area near the boundary, region A shows a better arrangement with an ORI of 74.9 %, and region B shows an ORI of 45.2 %, which can almost be considered as no orientation. Hence, besides the ORI, the size of region A needs to be considered to obtain the optimal parameters. To interpret the separation phenomenon, the finite element simulation (FES) of vacuum filtration was conducted. As shown in Fig. 4(b), 3D models were established with four different apertures (9 mm, 7 mm, 5 mm, 3 mm) to explore the change of flow field with different aperture's diameters. In the process of self-assembly, laminar flow will drive CFs to form a well-organized structure on account of the regular streamlines. In reverse, the turbulent flow will cause chaos because of the disordered flow. Fig. 4(c-f) present the flow fields of different apertures at 0.1 mm above the filtrating membrane, respectively, which could be regarded as the arrangement of CFs because of the tiny distance from the filtrating membrane. With the decrease of aperture diameter, the velocity of flow gradually increases, and the ordered area gradually shrinks with the edges starting to get disordered. In detail, as shown in Fig. 4(c), the streamlines start from the center point and end at the edge, which means that the fluid enters the aperture and leaves through the filtrating membrane. Different from Fig. 4(c), the flow field in Fig. 4(f) is divided into two parts by a boundary, which is in accordance with the experimental results. In the center region, the diffusion flow is still maintained with the streamlines starting from the center point. However, the streamlines of diffusion flow end at the boundary. In the edge of flow domain, the streamlines don't disappear directly, but reflux when crashing to the edge. To analyze the flow in detail, the flow fields of more cross sections are shown in Figure (g-l). Fig. 4(g) and 4(j) present the longitudinal section views and their enlarged views of 3 mm and 9 mm, respectively. Obviously, the flow is divided into upper and lower parts, as shown in Fig. 4(j). The lower part forms an ordered flow covering the whole filtrating membrane and the upper part forms vortexes, which will not influence the arrangement of CFs. However, as shown in Fig. 4(g), the stable and ordered flow only covers the region in the center. In the region near the edge, the fluid flow gets disordered and chaotic forming different flow fields. Fig. 4(h)(k) present the A-A cross-section views (at 1 mm above the filtrating membrane). In Fig. 4(h), the vortexes are formed because the fluid can't flow down but reflux when the flow crash to the edge. In contrast, most fluid flows regularly with a small number of disordered flows in Fig. 4 (k). These disordered flows don't originate from the edge but from the vortexes of the upper part shown in Fig. 4(j), which won't influence the flow of lower part. More information about the flow field is shown in Fig. S8 and S9. As a result, the reason for this phenomenon is that bigger in-plane velocity makes the time from the center to the edge decrease. However, the overall velocity of vacuum filtration stays the same for different apertures because the filtrating membrane pore doesn't change. Hence, the fluid can't flow down fast enough through the filtrating membrane for a smaller aperture, which results in the fluid reflux but not flowing down when the flow crash to the edge. Hence, the backflow and the coming flow crash into each other, forming the complex flow with a distinct boundary. In addition, Fig. 4(i)(l) present the streamlines of flow domain under the guide plate above the filtrating membrane, which are similar to the Ra/0.45/5-composite and Ra/0.80/7-composite, respectively, validating the accuracy of the simulation. Hence, during the self-assembly process, the diameter of aperture and the filtrating membrane pore will influence the size of the laminar flow area and determine whether there is a stable and ordered flow, by influencing the in-plane diffused velocity. Although the larger in-plane diffused velocity will give a better arrangement, the larger in-plane diffused velocity will reduce the size of the laminar flow area. Overall, 0.80 μm filtrating membrane pore and 7 mm aperture are chosen as the optimal parameters.

2.3. Characterization of thermal and mechanical properties

To analyze the thermal and mechanical properties of the prepared composites, a series of measurements, including laser flash analysis (LFA), differential scanning calorimetry (DSC), thermal gravimetric analysis (TG), thermal mechanical analysis (TMA), dynamic mechanical analysis (DMA) and tensile test, were carried out to explore the influence of parameters, respectively. First, the in-plane thermal diffusion coefficients (TD) of different composites obtained from LFA measurement are shown in Fig. 5(a). The in-plane TD of Ro/0.45/blank-composite is 6.879 mm^2/s, which is significantly higher than the pure PDMS (0.09 mm^2/s)), because the CFs tend to lie in plane (explained in Fig. S7) and the axial TD of CFs highly exceeds radial TD of CFs. However, in-plane random arrangement restricts the improvement of TD. With the addition of the guide plate, the TD highly increases with the highest TD reaching 23.1 mm^2/s because of the radial structure. The guide plate aperture and filtrating membrane pore will affect the in-plane diffused velocity of flow, the ORI of CFs, the mass fraction of CFs (explained in Fig. S7) and the integrity of composites (explained in Fig. S2). As a result, it's hard to summarize a general rule in the change of TD. Then, the thermogravimetric curves of some composites are shown in Fig. 5(b) from 25 ℃ to 1000 ℃ to calculate mass fractions of components. According to the weight loss ratio in the temperature range of 25 ℃ ~ 620 ℃ and 25 ℃ ~ 1000 ℃, the CFs' mass fraction of Ra/0.80/5-composite, Ra/0.80/7-composite, Ra/0.80/9-composite and Ro/0.45/blank-composite are 55.1%, 50.3%, 50.2% and 34.0 %, respectively (shown in Table S2 and Table S3). Ro/0.45/blank-composite shows a much lower mass fraction because random arrangement results in more holes in the scaffold, which partly accounts for the lower TD. Compared to that, in Ra/0.80/7-composite, more CFs can be deposited upon the filtrating membrane because of the regular and ordered arrangement, which brings a higher mass fraction than other three composites. Then the heat capacities and densities of some composites (shown in Table S4) were measured to calculate the TC, as shown in Fig. 5(c). Particularly, the in-plane TC of Ra/0.80/7-composite reaches 35.5 W/(m•K), showing 3.5 times that of Ro/0.45/blank-composite and 236 times that of pure PDMS. The highest anisotropy reaches 19.8, showing 2.8 times that of Ro/0.45/blank-composite. These improvements are attributed to the higher mass fraction of CFs and the excellent orientation of Ra/0.80/7-composite. Note that the thermal conductivity enhancement efficiencies (TCEE) of Ra/0.80/7-composite and Ro/0.45/blank-composite describe the efficiency of CFs per unit volume in contributing to the thermal enhancement, which is defined as:

$$TCEE = \frac{k - km}{100Vfkm} \tag{4}$$

Where k and k_m are the TC of the composite and pure PDMS, respectively. V_f represents the volume fraction of CFs in the composite. The in-plane TCEE of Ra/0.80/7-composite (6.5) is highly larger than that of Ro/0.45/blank-composite (3.2), validating the better heat transfer

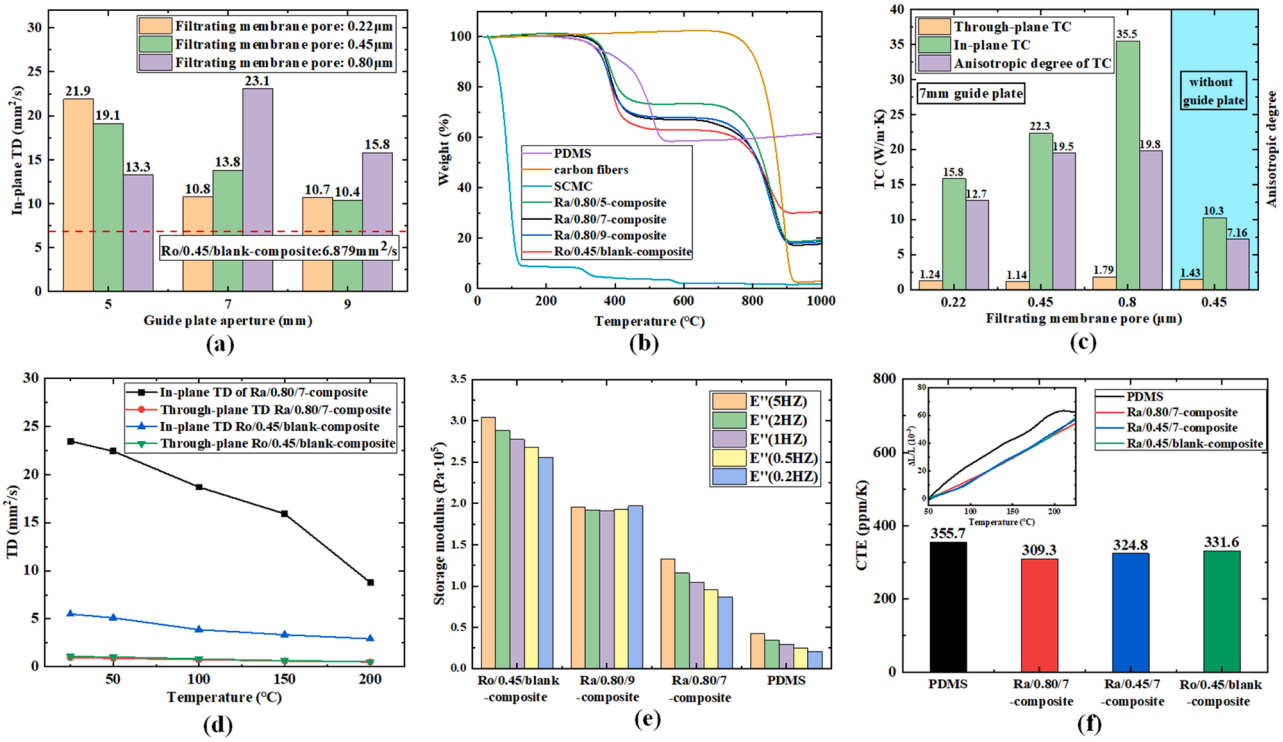

Fig. 5. (a) TD of different parameters. (b) The thermogravimetric curves of some composites. (c) TC of some composites. (d) The TD's changing curves of composites as the increase of temperature. (e) The storage modulus of some composites in different frequencies. (f) The CTE of PDMS, Ra/0.80/7-composite, Ra/0.45/7-composite and Ro/0.45/blank-composite between 50 ℃ and 250 ℃.

characteristic of CFs' pathways in Ra/0.80/7-composite. In addition, Fig. 5(d) presents the TD's changing curves of composites with the increase of temperature. Compared to Ro/0.45/blank-composite, the greater decrease in the in-plane TD of Ra/0.80/7-composite demonstrated that the anisotropy of CFs is taken full advantage of by the radial structure. It is worth mentioning that, in the composites made by vacuum filtration, CFs tend to lie along the in-plane direction, although they are disordered (Fig. S7), which makes the through-plane TC of composites show little difference.

Moreover, the mechanical properties were measured and compared between composites with radial and random structures. Fig. 5(e) illustrates the measuring result of DMA, showing the universal decrease of composites compared with pure PDMS because of the incorporation of CFs. Interestingly, Ra/0.80/7-composite shows less sacrifice in storage modulus than other composites because of the more regular orientation. The result of DMA is consistent with the result of tensile test in Fig. S11. Fig. 5(f) illustrates the coefficient of thermal expansion (CTE) of some composites between 50 ℃ and 250 ℃, which reflects the thermal stability. It is unusual that the CTE of composites are numerically close, showing a little enhancement compared to the PDMS. It is likely explained that, CFs are handled to be hydrophilic in the process of vacuum filtration, resulting in structural defects inside the composites when the matrix is filled in. All in all, via the above analysis of experimental results, Ra/0.80/7-composite shows better thermal and mechanical performances than others because of its better orientation.

2.4. Application and comparison of composites

Inspired by biological structures, the radial structure was proposed to solve the hotspot problem. To verify the effect of the radial structure, the finite element simulation (a more direct method to visualize the process of heat propagation) and thermal diffusion experiments were carried out. As shown in Fig. 6(a-c), temperature fields of composites with different CFs' structures were simulated, including random arrangement (a), radially oriented arrangement without connection (b) and radially oriented arrangement with sectional connection (c). A 1.5 mm diameter heat source was set in the center (detailed information is shown in Table S1). Fig. 6(d)(e) show the curves of maximum temperature and maximum temperature difference of three kinds of composites over time. Fig. 6(c) shows the lowest temperature in these composites, indicating its excellent heat transfer capacity in hotspots. To be specific, when the CFs connect with each other partially, continuous heat conduction channels are established, resulting in smaller contact thermal resistance (removing the thermal resistance between CFs and matrix), which maximally takes advantage of CFs' high axial TC. Moreover, Fig. 6(c) shows the lowest temperature difference, indicating that radial structure is much more beneficial to uniform heat conduction. The heat flow in Fig. 6(c) was uniformly and fast transferred from the center hotspot to the edge. However, the heat flow was restricted in a localized region in Fig. 6(a). As a result, the composite embedded with the radial oriented and connected structure of CFs demonstrated a fast and uniform heat-conduction capability, which is much superior to the random structure. To compare the actual heat transfer effect, Experiment I was designed and prepared to compare Ra/0.80/7-composite, Ro/0.45/blank-composite and commercial TIMs, whose experimental setup is shown in Fig. 6(g). 5 mm diameter ceramic heating sheets were used to simulate the hotspots and connected to a power supply in parallel. The surface temperatures of composites were recorded by a thermal infrared camera, and the core temperature of ceramic heating sheet was detected by thermocouples (Fig. S10). Fig. 6(f) presents the core temperature curves of ceramic heating sheets over time. The ceramic heating sheets with Ra/0.80/7-composite shows the lowest core temperature, which was 33.4 ℃ lower than that with commercial TIMs finally. In addition, Fig. 6(h) shows the infrared thermograms of composites' surfaces over time. It's worth noting that, Ra/0.80/7-composite shows the most uniform temperature field, however, Ro/0.45/blank-composite and commercial TIMs show a bigger temperature difference between the center and the edge. As a result, this experiment shows

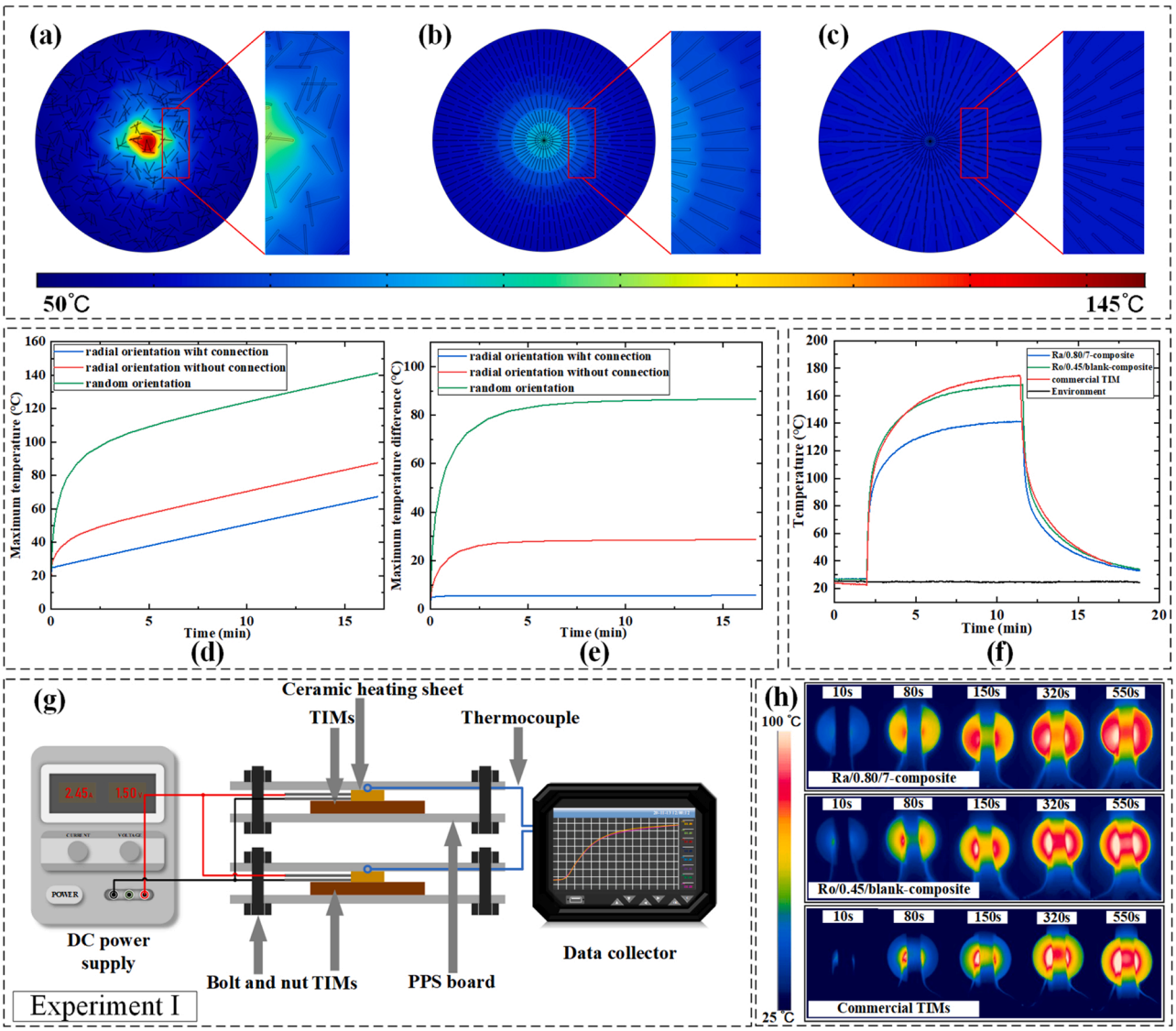

Fig. 6. Temperature field of composites with different CFs' structures including random arrangement (a), radially oriented arrangement without connection (b) and radially oriented arrangement with sectional connection (c). The curve of maximum temperature (d) and maximum temperature difference (e) of three kinds of composites over time. (f) The core temperature curve of the ceramic heating sheet over time. (g) The experimental setup for comparing the actual heat transfer effect. (h) The infrared thermograms of composites' surface over time.

consistent results to the simulation, indicating that Ra/0.80/7-composite (radial structure) has an excellent heat diffusion capacity for hotspots because of the establishment of heat pathways.

To verify the actual effect in heat dissipation system, experiment II was designed and conducted. Fig. 7(a) shows the typical heat dissipation device for chips with hotspots (Fig. S10). In this experiment, a 9 mm diameter ceramic heating sheet was selected to simulate the chip. To compare the heat dissipation effect in actual devices, four different materials were used in system as TIMs to connect the chip and heat sink, including PDMS, Ra/0.80/7-composite, Ro/0.45/blank-composite, and commercial TIMs. Thermocouples were used to detect the chip's core temperature, as shown in Fig. 7(e). The infrared thermograms of composites' surfaces were recorded by a thermal infrared camera, as shown in Fig. 7(b). Obviously, the system with Ra/0.80/7-composite shows the lowest chip temperature and the best temperature uniformity due to the radially oriented structure of CFs, which is conducive to guarantee the performance and lifetime of chips in practical application. As a result, Ra/0.80/7-composite shows terrific application potentiality in the heat dissipation of hotspots because of the radial structure inside.

In addition, the self-assembly strategy which combines vacuum filtration method and fluid control method can not only be used in the heat dissipation of local hotspots, but also is adaptive to arbitrary-shape heat sources. It is interesting that, as shown in Fig. 7(f), the special flow fields of "H", "U", "S", "T" were designed by machining the holes of corresponding glyphs. In theory, the arrangement of arbitrary two-dimensional shapes can be designed for heat sources of special shapes. Besides the hotspot problem, as shown in Fig. 7(d), the radial structure is also potential to be applied to solar-thermal-electric conversion because this special structure is contributory to absorb concentrated solar energy and transfer heat [36]. When phase change material (PCM) is incorporated in composites, the heat can spread rapidly and be absorbed in quantity. All in all, the flow field-driven self-assembly strategy proposed in this study is potential to be applied in lots of application prospects when the structure is designed properly.

3. Conclusion

In summary, we reported on a novel strategy combining vacuum filtration method and fluid control method to prepare the composites with the radial structure of CFs. To compare the degree of orientation

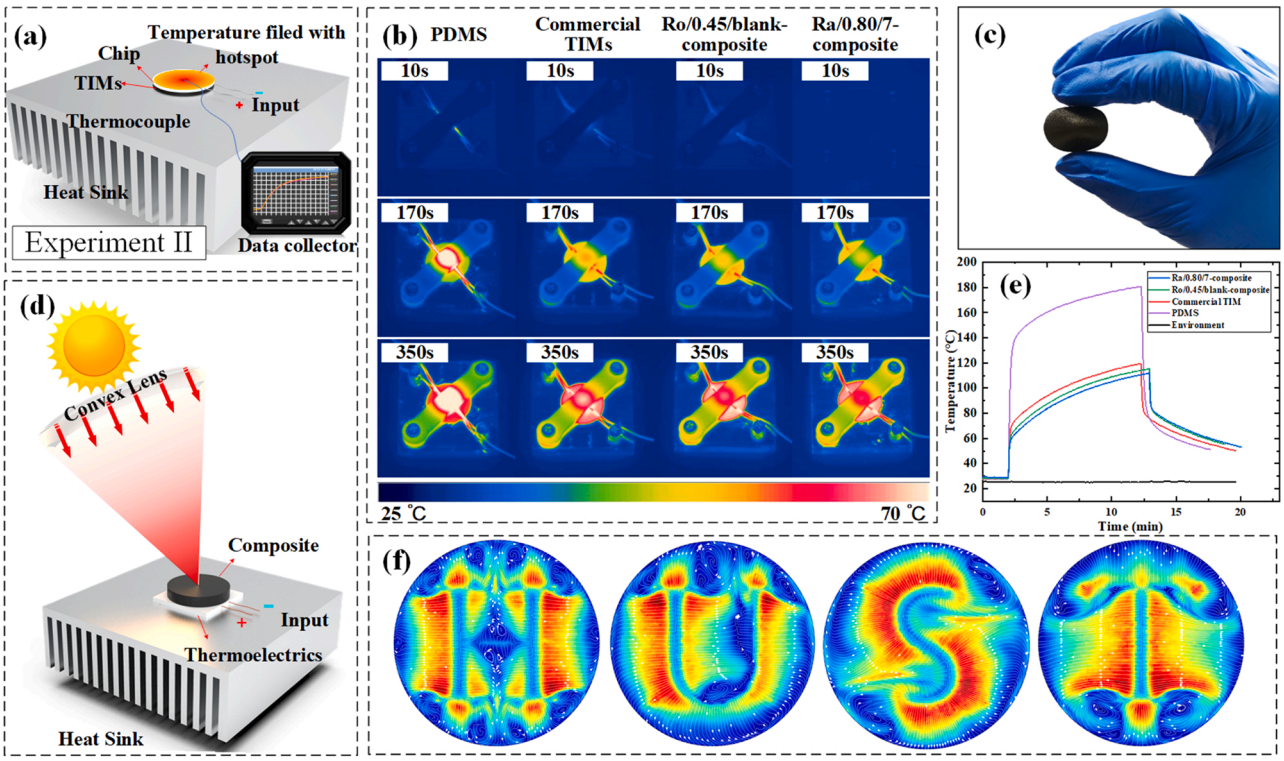

Fig. 7. (a) The experimental setup for comparing actual heat dissipation effect. (b) The infrared thermograms of composites' surface over time. (c) The photo of Ra/0.80/7-composite. (d) Schematic of the device for solar-thermal-electric conversion. (e) The core temperature curves of ceramic heating sheets over time. (f) The special flow fields of "H", "U", "S", "T".

quantitively, an orientation algorithm based on microscale image identification was developed and an evaluation criterion was proposed. Moreover, the flow field of vacuum filtration was simulated and analyzed to reveal the underlying orientation mechanisms of fillers under the driving of flow field. As a result, Ra/0.80/7-composite was prepared with the optimal parameters, demonstrating an ultrahigh in-plane TC of 35.5 W/(m•K) and ultrahigh TC anisotropy of 19.8 on account of the radially oriented structure of CFs. In addition, Ra/0.80/7-composite also demonstrated better mechanical performance and slightly superior thermal stability compared to randomly oriented composite. The radial structure of Ra/0.80/7-composite achieved fast and uniform heat transfer in the radial direction when applied in hotspots, which was validated by experimental results. Ra/0.80/7-composite demonstrated a broad application prospect of radially oriented composites in heat dissipation system. Moreover, this flow field-driven self-assembly strategy presents a promising self-design ability for the arrangement of arbitrary two-dimensional shapes and great potential in thermal interface materials and solar-thermal-electric conversion.

4. Experiment section

4.1. Materials

Carbon fibers (CFs) with a length of 200 μm (K223HM) and axial thermal conductivities of 600 W/(m•K) were purchased from Mitsubishi Chemical. Hexadecyl trimethyl ammonium Bromide (CTAB) was purchased from Aladdin and used as a cationic surface-active agent. The Sodium Carboxymethyl Cellulose (SCMC) was purchased from Aladdin and used as a binder to bind CFs. Polydimethylsiloxane (PDMS) was purchased from Dow Corning Co., Ltd. and used as the polymer matrix. All chemicals were directly used without further purification. Mixed cellulose Esters (MCE, made of nitrocellulose and cellulose acetate) filtrating membranes of different pores were purchased from Shanghai Xinya purification device manufacturer, which have a good mechanical strength, toughness and temperature stability (Maximum operating temperature of 130 ℃). Guide plates were obtained by CNC machining.

4.2. Synthesis of radially and randomly oriented-CFs scaffolds

First, to promote the hydrophilia and dispersibility of CFs in solution, 0.25 g CFs and 0.02 g CTAB were added into 100 ml deionized water and stirred in magnetic stirring apparatus for 10 min, forming mixture A. Second, 200 ml of deionized water was added into the upper flask as preset water to slow down the sedimentation of CFs and create a stable initial flow field under the guide plate. Third, mixture A was added into the preset water of the upper flask, forming mixture B. After a while, until the flow of mixture B weaken (to relieve the influence of the existing flow on the flow field under the guide plate), the vacuum pump was started to force deionized water flow through the filtrating membrane. Meanwhile, CFs were forced to be deposited on the filtrating membrane, obeying the feature of flow field. Fourthly, after all CFs had been deposited, 15 ml of SCMC solution (1.5 wt%) was dropped into the upper flask with vacuum filtration sustaining 15 min, which ensured SCMC enwind the CFs. Fifthly, after all deionized water was pumped out, the composite of state-A was frozen upon a copper cylinder with liquid nitrogen in the bottom. After that, the composite of state-A was transferred to a freeze-dryer and sustained 24 h of vacuum-assisted freeze-drying (−60 ℃, <10 Pa), obtaining the CFs scaffold (state-B). Specifically, the radially oriented-CFs scaffold was obtained when the guide plate was assembled into the upper flask. The randomly oriented-CFs scaffold was obtained when the guide plate was removed.

4.3. Fabrication of CFS/PDMS composites

First, PDMS was prepared by mixing component A and component B by 10:1. Then alternating cycles of vacuum were applied in the mixed PDMS to remove bubbles. Second, PDMS was slowly poured into the

scaffold, and continuous degassing was carried out every 5 min. This process was carried out repeatedly for 5 times to ensure that PDMS was fully impregnated into the scaffold. In this process, freeze-dried SCMC played a role in fixing CFs and preventing the scaffold from disintegrating due to air bubbles. Third, when air bubbles were no longer produced, the redundant PDMS upon the scaffold was discreetly scraped off and squeezed out. After that, a thermal treatment step at 70 ℃ for 3 h was conducted to ensure the full curing of the composites. Composites with radially oriented CFs and randomly oriented CFs were prepared, respectively.

4.4. Characterization

The microscopic morphology was tested by a field-emission scanning electron microscope (FSEM, Sirion 200) to characterize the morphologies of scaffolds and cross-section of composites at an accelerating voltage of 10 kV. The SEM images of scaffolds were used to calculate the degree of orientation (ORI) by applying an orientation algorithm based on microscale image identification. The sectional SEM images of composites were shown to intuitively compare their orientations in support information. Thermogravimetric analysis (TG, TGA8000) was carried out to verify the mass fraction of each component, which can be calculated according to the equation: $\Delta M = W_{PDMS} \times \Delta M_{PDMS} + W_{SCMC} \times \Delta M_{SCMC} + W_{CFs} \times \Delta M_{CFs}$, where ΔM, ΔM_{PDMS}, ΔM_{SCMC} and ΔM_{CFs} correspond to the weight loss ratio of each component in a temperature range, respectively. W_{PDMS}, W_{SCMC} and W_{CFs} correspond to the mass fraction of each component. In-plane TC and through-plane TC were calculated according to the equation $\kappa = \alpha \times \rho \times C$, where κ, α, ρ, and C correspond to TC, TD, density, and specific heat capacity, respectively. The in-plane and through-plane TD of composites were measured by LFA 467 (Netzsch). The specific heat capacities of composites were measured by differential scanning calorimetry (Diamond DSC, PerkinElmer Instruments). In addition, the CTE of the composites in the through-plane direction were measured by static thermomechanical analysis (TMA, Q400EM) with a temperature range from 35 ℃ to 250 ℃. The storage moduli of composites were measured by dynamic thermomechanical analysis (Diamond DMA) in compress mode. The tensile tests of composites were measured with a loading rate of 1 mm min^{-1} by Instron 5943.

CRediT authorship contribution statement

Xinfeng Zhang: Conceptualization, Methodology, Software, Validation, Formal analysis, Investigation, Data curation, Writing – original draft, Writing – review & editing, **Bin Xie**: Conceptualization, Resources, Writing – review & editing, Funding acquisition, **Shuling Zhou**: Investigation, Methodology, Writing – review & editing; **Xuan Yang**: Resources, Methodology, Formal analysis, **Yiwen Fan**: Formal analysis, Validation, Software, **Run Hu**: Supervision, Funding acquisition, Writing – review & editing, **Xiaobing Luo*** : Conceptualization, Project administration, Funding acquisition, Writing – review & editing.

Declaration of Competing Interest

The authors declare that they have no known competing financial interests or personal relationships that could have appeared to influence the work reported in this paper.

Data availability

Data will be made available on request.

Acknowledgments

This work is supported by the National Natural Science Foundation of China (51625601, 52106089, 52076087).

Appendix A. Supporting information

Supplementary data associated with this article can be found in the online version at doi:10.1016/j.nanoen.2022.107986.

References

[1] A.L. Moore, L. Shi, Emerging challenges and materials for thermal management of electronics, Mater. Today 17 (4) (2014) 163–174.
[2] B.C. Liu, Y.B. Li, T. Fei, et al., Highly thermally conductive polystyrene/polypropylene/boron nitride composites with 3D segregated structure prepared by solution-mixing and hot-pressing method, Chem. Eng. J. 385 (2020), 123829.
[3] X. Zhang, K. Wu, Y.H. Liu, et al., Preparation of highly thermally conductive but electrically insulating composites by constructing a segregated double network in polymer composites, Compos. Sci. Technol. 175 (2019) 135–142.
[4] N.Y. Ning, S.R. Fu, W. Zhang, et al., Realizing the enhancement of interfacial interaction in semicrystalline polymer/filler composites via interfacial crystallization, Prog. Polym. Sci. 37 (10) (2012) 1425–1455.
[5] D. Suh, C.M. Moon, D. Kim, et al., Ultrahigh thermal conductivity of interface materials by silver-functionalized carbon nanotube phonon conduits, Adv. Mater. 28 (33) (2016) 7220–7227.
[6] S. Stankovich, D.A. Dikin, G.H.B. Dommett, et al., Graphene-based composite materials, Nature 442 (7100) (2006) 282–286.
[7] H.Y. Chen, V.V. Ginzburg, J. Yang, et al., Thermal conductivity of polymer-based composites: Fundamentals and applications, Prog. Polym. Sci. 59 (2016) 41–85.
[8] J.N. Coleman, U. Khan, W.J. Blau, et al., Small but strong: a review of the mechanical properties of carbon nanotube-polymer composites, Carbon 44 (9) (2006) 1624–1652.
[9] D. Garlotta, A literature review of poly(lactic acid), J. Polym. Environ. 9 (2) (2001) 63–84.
[10] Y.B. Tao, H.L. Wang, Z.L. Li, et al., Development and application of wood flour-filled polylactic acid composite filament for 3D printing, Materials 10 (4) (2017) 339.
[11] A. Anis, A.Y. Elnour, M.A. Alam, et al., Aluminum-filled amorphous-PET, a composite showing simultaneous increase in modulus and impact resistance, Polymers 12 (9) (2020) 2038.
[12] C.H. Huang, S.B. Wang, L.G. Liu, Experimental study on the mechanical properties of metal oxides filled PA1010 composites, Key Eng. Mater. 353–358 (2007) 1346–1349.
[13] P. Minakshi, H. Mohan, Manjeet, et al., Organic polymer and metal nano-particle based composites for improvement of the analytical performance of electrochemical biosensor, Curr. Top. Med. Chem. 20 (11) (2020) 1029–1041.
[14] W.L. Song, P. Wang, L. Cao, et al., Polymer/boron nitride nanocomposite materials for superior thermal transport performance, Angew. Chem. Int. Ed. 51 (26) (2012) 6498–6501.
[15] S. Al-Jawoosh, A. Ireland, B. Su, Fabrication and characterisation of a novel biomimetic anisotropic ceramic/polymer-infiltrated composite material, Dent. Mater. 34 (7) (2018) 994–1002.
[16] Y. Wu, Y. Xue, S. Qin, et al., BN nanosheet/polymer films with highly anisotropic thermal conductivity for thermal management applications, ACS Appl. Mater. Interfaces 9 (49) (2017) 43163–43170.
[17] J. Wang, Y. Wu, Y. Xue, et al., Super-compatible functional boron nitride nanosheets/polymer films with excellent mechanical properties and ultra-high thermal conductivity for thermal management, J. Mater. Chem. C 6 (6) (2018) 1363–1369.
[18] J. Wang, Q. Li, D. Liu, et al., High temperature thermally conductive nanocomposite textile by "green" electrospinning, Nanoscale 10 (35) (2018) 16868–16872.
[19] A. Kasar, G.P. Xiong, P.L. Menezes, Graphene-reinforced metal and polymer matrix composites, JOM 70 (6) (2018) 829–836.
[20] C.X. Lei, Y.Z. Zhang, D.Y. Liu, et al., Highly thermo-conductive yet electrically insulating material with perpendicularly engineered assembly of boron nitride nanosheets, Compos. Sci. Technol. 214 (2021), 108995.
[21] K. Uetani, S. Ata, S. Tomonoh, et al., Elastomeric thermal interface materials with high through-plane thermal conductivity from carbon fiber fillers vertically aligned by electrostatic flocking, Adv. Mater. 26 (33) (2014) 5857–5862.
[22] C. Yuan, B. Duan, L. Li, et al., Thermal conductivity of polymer-based composites with magnetic aligned hexagonal boron nitride platelets, ACS Appl. Mater. Interfaces 7 (23) (2015) 13000–13006.
[23] J. Hansson, T.M.J. Nilsson, L. Ye, et al., Novel nanostructured thermal interface materials: a review, Int. Mater. Rev. 63 (1) (2017) 22–45.
[24] H. Ma, B. Gao, M. Wang, et al., Strategies for enhancing thermal conductivity of polymer-based thermal interface materials: a review, J. Mater. Sci. 56 (2) (2020) 1064–1086.
[25] C. Lei, Z. Xie, K. Wu, et al., Controlled vertically aligned structures in polymer composites: natural inspiration, structural processing, and functional application, Adv. Mater. 33 (49) (2021) 2103495.
[26] X.L. Zeng, Y.M. Yao, Z.Y. Gong, et al., Ice-templated assembly strategy to construct 3D boron nitride nanosheet networks in polymer composites for thermal conductivity improvement, Small 11 (46) (2015) 6205–6213.
[27] J. Wang, D. Liu, Q. Li, et al., Lightweight, superelastic yet thermoconductive boron nitride nanocomposite aerogel for thermal energy regulation, ACS Nano 13 (7) (2019) 7860–7870.

[28] X. Ge, J.Y. Zhang, G.Q. Zhang, et al., Low melting-point alloy-boron nitride nanosheet composites for thermal management, ACS Appl. Nano Mater. 3 (4) (2020) 3494–3502.
[29] R. Tutika, S. Kmiec, A.B.M.T. Haque, et al., Liquid metal-elastomer soft composites with independently controllable and highly tunable droplet size and volume loading, ACS Appl. Mater. Interfaces 11 (19) (2019) 17873–17883.
[30] P. Liu, Y.Y. Luo, J.M. Liu, et al., Laminar metal foam: a soft and highly thermally conductive thermal interface material with a reliable joint for semiconductor packaging, ACS Appl. Mater. Interfaces 13 (13) (2021) 15791–15801.
[31] A. Bar-Cohen, P. Wang, Thermal management of on-chip hot spot, J. Heat. Trans-T, J. Heat Trans. 134 (5) (2012), 051017.
[32] J.K. Han, G.L. Du, W.W. Gao, et al., An anisotropically high thermal conductive boron nitride/epoxy composite based on nacre-mimetic 3D network, Adv. Funct. Mater. 29 (13) (2019) 1900412.
[33] Y.J. Wang, S. Xia, H. Li, et al., Unprecedentedly tough, folding-endurance, and multifunctional graphene-based artificial nacre with predesigned 3D nanofiber network as matrix, Adv. Funct. Mater. 29 (38) (2019) 1903876.
[34] U.G.K. Wegst, H. Bai, E. Saiz, et al., Bioinspired structural materials, Nat. Mater. 14 (1) (2015) 23–36.
[35] J. Wang, D. Liu, Q. Li, et al., Nacre-bionic nanocomposite membrane for efficient in-plane dissipation heat harvest under high temperature, J. Mater. 7 (2) (2021) 219–225.
[36] D. Liu, C. Lei, K. Wu, et al., A multidirectionally thermoconductive phase change material enables high and durable electricity via real-environment solar-thermal-electric conversion, ACS Nano 14 (11) (2020) 15738–15747.
[37] W.Z. Xu, Y. Xing, J. Liu, et al., Efficient water transport and solar steam generation via radially, hierarchically structured aerogels, ACS Nano 13 (7) (2019) 7930–7938.
[38] C.H. Wang, X. Chen, B. Wang, et al., Freeze-casting produces a graphene oxide aerogel with a radial and centrosymmetric structure, ACS Nano 12 (6) (2018) 5816–5825.
[39] Z. Bo, H.R. Zhu, C.Y. Ying, et al., Tree-inspired radially aligned, bimodal graphene frameworks for highly efficient and isotropic thermal transport, Nanoscale 11 (44) (2019) 21249–21258.
[40] K. Xie, Y.H. Liu, Y.X. Tian, et al., Improving the flexibility of graphene nanosheets films by using aramid nanofiber framework, Compos. Part A-Appl. S 142 (2021), 106265.
[41] X.L. Zeng, J.J. Sun, Y.M. Yao, et al., A combination of boron nitride nanotubes and cellulose nanofibers for the preparation of a nanocomposite with high thermal conductivity, ACS Nano 11 (5) (2017) 5167–5178.
[42] X.W. He, W.L. Gao, L.J. Xie, et al., Wafer-scale monodomain films of spontaneously aligned single-walled carbon nanotubes, Nat. Nanotechnol. 11 (7) (2016) 633–639.
[43] V. Krishnan, Y. Kasuya, Q. Ji, et al., Vortex-aligned fullerene nanowhiskers as a scaffold for orienting cell growth, ACS Appl. Mater. Interfaces 7 (28) (2015) 15667–15673.